Crystal structure, chemical bond characteristics, infrared reflection spectrum, and microwave dielectric properties of $Nd_2(Zr_{1-x}Ti_x)_3(MoO_4)_9$ ceramics

Jian BAO^a, Yuping ZHANG^a, Hideo KIMURA^a, Haitao WU^{a,*}, Zhenxing YUE^{b,*}

^{a}*School of Environmental and Material Engineering, Yantai University, Yantai 264005, China*
^{b}*State Key Laboratory of New Ceramics and Fine Processing, School of Materials Science and Engineering, Tsinghua University, Beijing 100084, China*

Abstract: Microwave dielectric ceramics (MWDCs) with low dielectric constant and low dielectric loss are desired in contemporary society, where the communication frequency is developing to high frequency (sub-6G). Herein, $Nd_2(Zr_{1-x}Ti_x)_3(MoO_4)_9$ ($NZ_{1-x}T_xM$, x = 0.02–0.10) ceramics were prepared through a solid-phase process. According to X-ray diffraction (XRD) patterns, the ceramics could form a pure crystal structure with the $R\bar{3}c$ (167) space group. The internal parameters affecting the properties of the ceramics were calculated and analyzed by employing Clausius–Mossotti relationship, Shannon's rule, and Phillips–van Vechten–Levine (P–V–L) theory. Furthermore, theoretical dielectric loss of the ceramics was measured and analyzed by a Fourier transform infrared (IR) radiation spectrometer. Notably, when x = 0.08 and sintered at 700 ℃, optimal microwave dielectric properties of the ceramics were obtained, including a dielectric constant (ε_r) = 10.94, $Q{\cdot}f$ = 82,525 GHz (at 9.62 GHz), and near-zero resonant frequency temperature coefficient (τ_f) = −12.99 ppm/℃. This study not only obtained an MWDC with excellent properties but also deeply analyzed the effects of Ti^{4+} on the microwave dielectric properties and chemical bond characteristics of $Nd_2Zr_3(MoO_4)_9$ (NZM), which laid a solid foundation for the development of rare-earth molybdate MWDC system.

Keywords: microwave dielectric ceramics (MWDCs); $Nd_2(Zr_{1-x}Ti_x)_3(MoO_4)_9$ ($NZ_{1-x}T_xM$); Phillips–van Vechten–Levine (P–V–L) theory; theoretical dielectric loss

1 Introduction

With the development of Internet of Things, Augmented Reality (AR) remote cooperation, and other technologies, high-speed communication network, such as the fifth-generation (5G) mobile network, is in the spotlight. Currently, many passive devices composed of microwave dielectric ceramics (MWDCs) play a major role in the 5G technology [1–4]. To meet the urgent demand for the 5G communication technology, the ceramic materials with excellent performance are expected. Generally, the ceramics with practical application potential meet the following aspects, including a small dielectric constant (ε_r), a good quality factor ($Q{\cdot}f$), and a near-zero resonant frequency temperature coefficient (τ_f) [5–8].

In addition, the passive components with low sintering temperatures show low production costs and high market competitiveness, which are also conducive to energy conservation and emission reduction. Therefore, the ceramics with good microwave dielectric properties and low sintering temperatures should be studied.

Over the years, Mo-based MWDCs have been widely studied by researchers, such as $Na_2O–MoO_3$ binary system, $K_2O–MoO_3$ binary system, and $Na_2O–Bi_2O_3–MoO_3$ ternary system [9–13]. Moreover, $Ln_2Zr_3(MoO_4)_9$ ceramics (rare-earth molybdate system) have become the focus due to the low sintering temperatures. Table 1 shows the microwave dielectric properties of the $Ln_2Zr_3(MoO_4)_9$ ceramics [14–21]. High dielectric loss of $Nd_2Zr_3(MoO_4)_9$ (NZM) limits the application potential for microwave communication devices. Before the modification experiment, an undoped NZM ceramics matrix was prepared, and the microwave dielectric properties of the ceramics are listed in Fig. S1 in the Electronic Supplementary Material (ESM). The $Q·f$ value of the NZM is relatively poor in the $Ln_2Zr_3(MoO_4)_9$ ceramics. Therefore, it is of interest to explore a practical and effective method to improve the $Q·f$ value of the NZM.

Refs. [22,23] show that the dielectric loss of the ceramics can be reduced by adding appropriate ions. Feng *et al.* [24] improved the $Q·f$ value by the partial replacement of Zr^{4+} by $(Al_{1/2}Ta_{1/2})^{4+}$ ions in $Ce_2Zr_3(MoO_4)_9$ ceramics. In addition, $Ce_2(Zr_{1−x}(Mn_{1/3}Sb_{2/3})_x)_3(MoO_4)_9$ ceramics [25] and $Ce_2(Zr_{1−x}(Al_{1/2}Nb_{1/2})_x)_3(MoO_4)_9$ ceramics [26] also exhibited good dielectric properties. Therefore, the Zr-site was selected as the site for ion doping instead of choosing Nd-site and Mo-site. Herein, a series of $Nd_2(Zr_{1−x}Ti_x)_3(MoO_4)_9$ ($NZ_{1−x}T_xM$, $x = 0.02–0.10$) ceramics were fabricated. Ti^{4+} was employed to replace Zr^{4+} in NZM ceramics for the first time. The dielectric loss of the ceramics is significantly reduced. In addition, the effects of Ti^{4+} on the microwave dielectric properties and the crystal structure of the NZM are studied. The internal factors affecting the properties of $NZ_{1−x}T_xM$ are revealed through Phillips–van Vechten–Levine (P–V–L) theory [27].

2 Experimental procedure

In this experiment, high-purity powders including Nd_2O_3 (99.99%, Aladdin), ZrO_2 (99.99%, Aladdin), MoO_3 (99.95%, Aladdin), and TiO_2 (99.99%, Aladdin) were used to synthesize $NZ_{1−x}T_xM$ ($x = 0.02–0.10$) ceramics by a solid-phase process [28–30]. The raw powders with precise weight were put into a ball mill tank with ZrO_2 and C_2H_5OH, and then ground with a ball mill for 12 h. After drying at 65 ℃, these powders were calcined at 700 ℃ for 2 h in air. Subsequently, 10% polyvinyl alcohol (PVA) was placed in the calcined powders. The quantitative powders were pressed in a cylindrical mold to produce green bodies (the height and diameter are 6 and 10 mm, respectively). Finally, the green bodies were sintered from 775 to 875 ℃ for 4 h.

The phases of $NZ_{1−x}T_xM$ were revealed by an X-ray diffractometer (D/MAX-B, Rigaku, Japan), and much more information was obtained by Rietveld refinement. Stomata distributions and grain morphologies of the samples were studied by a scanning electron microscope (SEM; S-4800, Hitachi, Japan). Reflectance spectra of $NZ_{1−x}T_xM$ in far-infrared (IR) and mid-IR bands were measured through a Fourier transform IR radiation spectrometer (IFS 66v, Bruker, Germany) at National Synchrotron Radiation Laboratory (NSRL). All the

Table 1 Microwave dielectric properties of $Ln_2Zr_3(MoO_4)_9$ ceramics

Material	Temperature (℃)	ε_r	$Q·f$ (GHz)	τ_f (ppm/℃)	Ref.
$Eu_2Zr_3(MoO_4)_9$	600	10.75	74,900	−8.88	[14]
$Sm_2Zr_3(MoO_4)_9$	875	11.00	74,012	−45.30	[15]
NZM	850	10.80	58,942	−40.90	[15]
$Pr_2Zr_3(MoO_4)_9$	650	10.72	64,200	−13.00	[16]
$La_2Zr_3(MoO_4)_9$	775	10.80	50,628	−38.80	[17]
$Gd_2Zr_3(MoO_4)_9$	725	10.78	40,945	−12.26	[18]
$Ce_2Zr_3(MoO_4)_9$	575	10.69	19,062	−1.29	[19]
$Ce_2(Zr_{0.92}Sn_{0.08})_3(MoO_4)_9$	700	10.22	72,390	−7.54	[20]
$Ce_2(Zr_{0.96}(Co_{1/2}W_{1/2})_{0.04})_3(MoO_4)_9$	750	9.95	80,803	−9.10	[21]
$Nd_2(Zr_{0.92}Ti_{0.08})_3(MoO_4)_9(NZ_{0.92}T_{0.08}M)$	700	10.94	82,525	−12.99	This work

properties of the $NZ_{1-x}T_xM$ ceramics were measured through a vector network analyzer (N5234A, Agilent, USA). The microwave dielectric properties of the $NZ_{1-x}T_xM$ ceramics were measured by $TE_{01\delta}$ resonator mode. Among them, the ε_r was measured between two large metal plates according to Hakki–Coleman method [31], and the $Q \cdot f$ was measured through resonant cavity method in a closed metal cavity [32,33]. The resonant frequencies at different temperatures were measured, and Eq. (1) was employed to calculate the τ_f of the ceramics [34,35].

$$\tau_f = \frac{f_1 - f_0}{f_0(T_1 - T_0)} \quad (1)$$

where f_0 is the resonant frequency at 25 ℃ (T_0), and f_1 is the resonant frequency at 85 ℃ (T_1).

3　Results and discussion

The XRD data of the $NZ_{1-x}T_xM$ (x = 0.02–0.10) ceramics are demonstrated in Fig. 1. Crystal lattice parameters and refinement parameters of the ceramics are presented in Table 2. Standard PDF card ($Pr_2Zr_3(MoO_4)_9$, PDF Card No. 51-1851) is used to compare the ceramics' diffraction patterns. Over the entire doping range, all diffraction peaks correspond well with the PDF card. The results demonstrate that the $NZ_{1-x}T_xM$ solid solution with the $R\overline{3}c$ (167) space group is formed, and the addition of Ti^{4+} does not produce a secondary phase. In addition, when x = 0.02–0.08, the relative intensities of partial diffraction peaks (2θ = 27.327° and 27.769°) of the samples are different from those of the PDF card. The reason for the difference may be the inherent difference between the $Pr_2Zr_3(MoO_4)_9$ card and the $NZ_{1-x}T_xM$ samples, or caused by the preferred orientation coming from an unidirectional pressure in the preparation process. Crystallographic information file (CIF; NZM, Inorganic Crystal Structure Database (ICSD)#92600) is chosen

as a model in Fullprof program. Bond lengths for each chemical bond obtained by the Rietveld refinement are exhibited in Table S1 in the ESM. As shown in Table 2, the values of the reliability factors of pattern (R_p) and weighted pattern (R_{wp}) of $NZ_{1-x}T_xM$ are less than 10%, proving that the results were credible. Figure 2 is plotted to make the refinement results more readable. The lattice volume of the samples decreases linearly with the increase of the x value due to the ionic radius of Ti^{4+} (0.605 Å) being smaller than that of Zr^{4+} (0.72 Å).

CrystalMaker software is used to draw a three-dimensional (3D) crystal cell diagram of the (001) and (110) sides of $NZ_{1-x}T_xM$, as exhibited in Fig. 3. Three types of coordination polyhedrons of Nd–O, Zr(Ti)–O, and Mo–O are seen clearly. In this structure, all the O^{2-} anions occupy the $36f$ Wyckoff positions, and Nd^{3+}, $Zr(Ti)1^{4+}$, $Zr(Ti)2^{4+}$, $Mo1^{6+}$, and $Mo2^{6+}$ cations occupy the $12c$, $6b$, $12c$, $36f$, and $18e$ Wyckoff positions, respectively [36]. Among them, Mo atoms have a tetrahedral oxygen environment with Mo1 in the general position and Mo2 in the two-fold axis. The average bond lengths of the Mo–O bond are 1.7529 and 1.8461 Å. Two separate Zr(Ti) atoms lie on the three-fold axis inside the oxygen octahedra. The
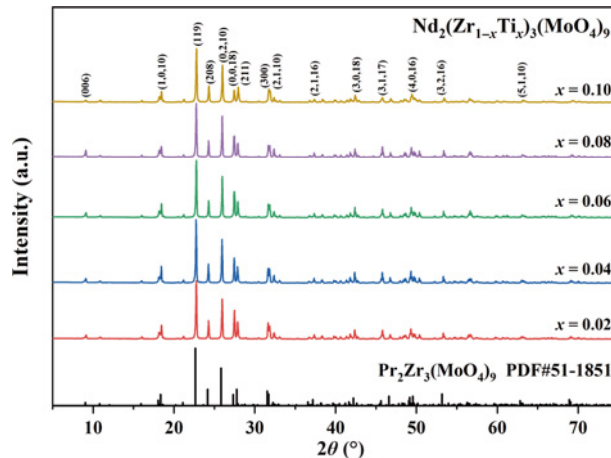

Fig. 1　XRD patterns of $NZ_{1-x}T_xM$ (x = 0.02–0.10) ceramics sintered at optimal temperatures.

Table 2　Crystal lattice parameters and reliability factors of $NZ_{1-x}T_xM$ (x = 0.02–0.10) ceramics sintered at optimal temperatures

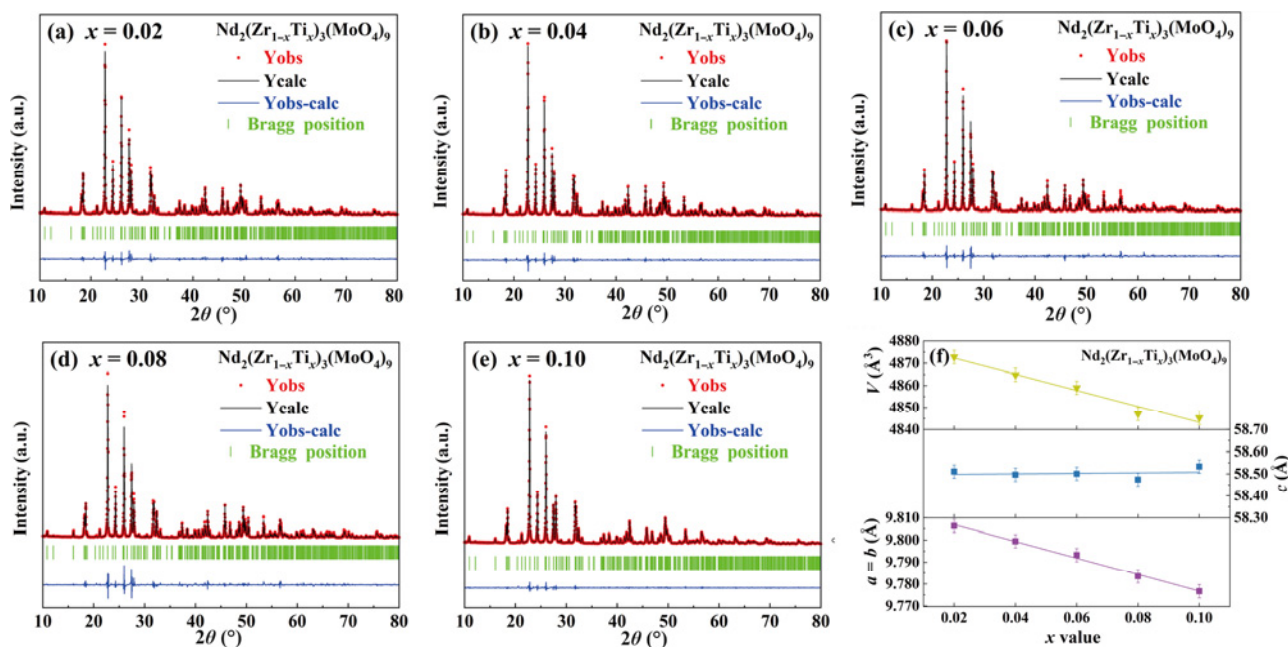| x value	Crystal lattice parameter					Reliability fator	
	a and b (Å)	c (Å)	α and β (°)	γ (°)	Molar volume V (Å³)	R_p (%)	R_{wp} (%)
0.02	9.8063	58.5110	90	120	4872.824	5.64	7.40
0.04	9.7995	58.4966	90	120	4864.796	4.94	6.63
0.06	9.7932	58.5010	90	120	4858.996	5.99	7.91
0.08	9.7835	58.4743	90	120	4847.131	6.65	8.71
0.10	9.7767	58.5337	90	120	4845.306	3.61	4.87

Fig. 2 (a–e) Rietveld refinement plots of $NZ_{1-x}T_xM$ (x = 0.02–0.10) and (f) cell parameters of $NZ_{1-x}T_xM$ (x = 0.02–0.10).
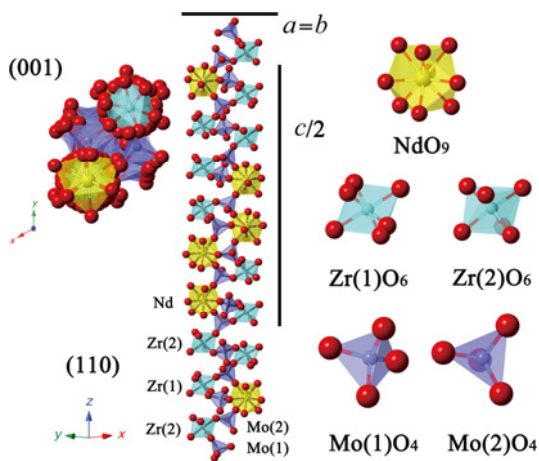

Fig. 3 Refined crystal structures of $NZ_{1-x}T_xM$ (x = 0.02–0.10) ceramics.

average bond lengths of the Zr(Ti)–O bond are 2.1546 and 2.0770 Å. The average bond length of the Nd–O bond is 2.5115 Å. The Nd atom forms a polyhedron with nine oxygen atoms, which is common in rare earth elements. The three polyhedrons form $NZ_{1-x}T_xM$ crystals through the co-top connection.

Figure 4 shows the SEM photographs of the $NZ_{1-x}T_xM$ ceramics sintered at the optimal temperatures. The surfaces of all samples show clear grain boundaries and no obvious pores, indicating that the samples have reached a dense state. Figure 5 shows the grain size distributions of the samples collected and analyzed by Nano Measurer and Origin programs, respectively. The mean size of the grains increases from 0.6361 to

1.3108 μm with the increase of the Ti^{4+} content. It is worth mentioning that when the x value reaches 0.1, the standard deviation of the grain size distribution of the sample is significantly greater than those of other samples, indicating that the grain size distribution is more discrete. The uneven distribution of the grain size may deteriorate the dielectric properties of the samples.

The ε_r is a physical quantity to measure the polarization ability of the MWDCs, which is demonstrated in Fig. 6(a). The ε_r of the ceramics depends on intrinsic parameters and extrinsic parameters [37]. Hence, the apparent densities and relative densities ($\rho_{relative}$) of the samples are measured and plotted in Figs. 6(b) and 6(c), respectively. As is well known, the ε_r of the samples is much larger than that of air (ε = 1). With the increase of the sintering temperatures, the pores in the samples are expelled, and both densities and ε_r of the samples increase. Furthermore, as shown in Fig. 6(c), the $\rho_{relative}$ of the samples is about 94% at the optimal sintering temperature. It is necessary to exclude the influence of residual trace pores.

According to Bosman–Havinga equation [38], the stoma correction dielectric constant ($\varepsilon_{corr.}$) is calculated.

$$\varepsilon_{corr.} = \varepsilon_r(1+1.5P) \qquad (2)$$

$$P = 1 - \rho_{relative} \qquad (3)$$

where P is the porosity of the samples. Figure 7 shows the ε_r and the $\varepsilon_{corr.}$ of the samples sintered at the optimal temperatures. The ε_r and the $\varepsilon_{corr.}$ exhibit a
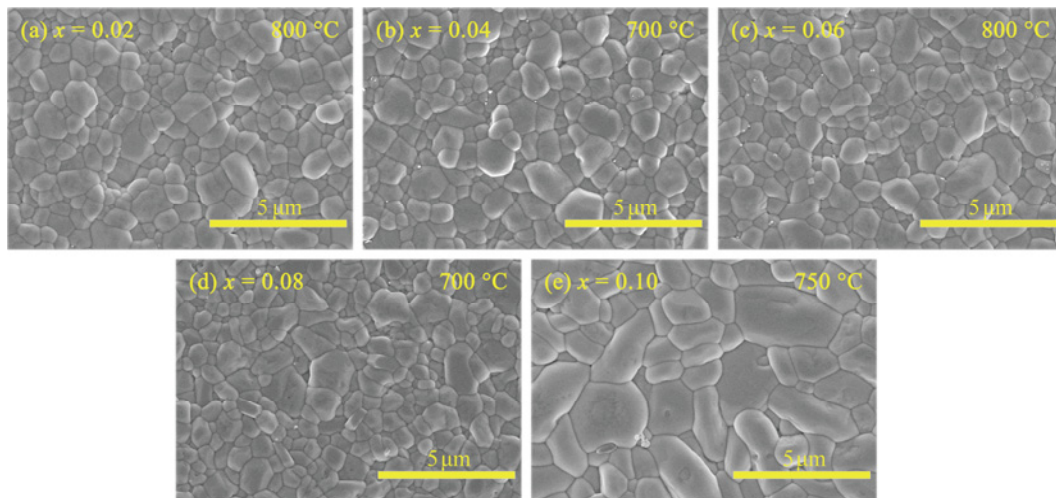
Fig. 4 SEM photographs of NZ$_{1-x}$T$_x$M (x = 0.02–0.10) ceramics sintered at optimal temperatures.
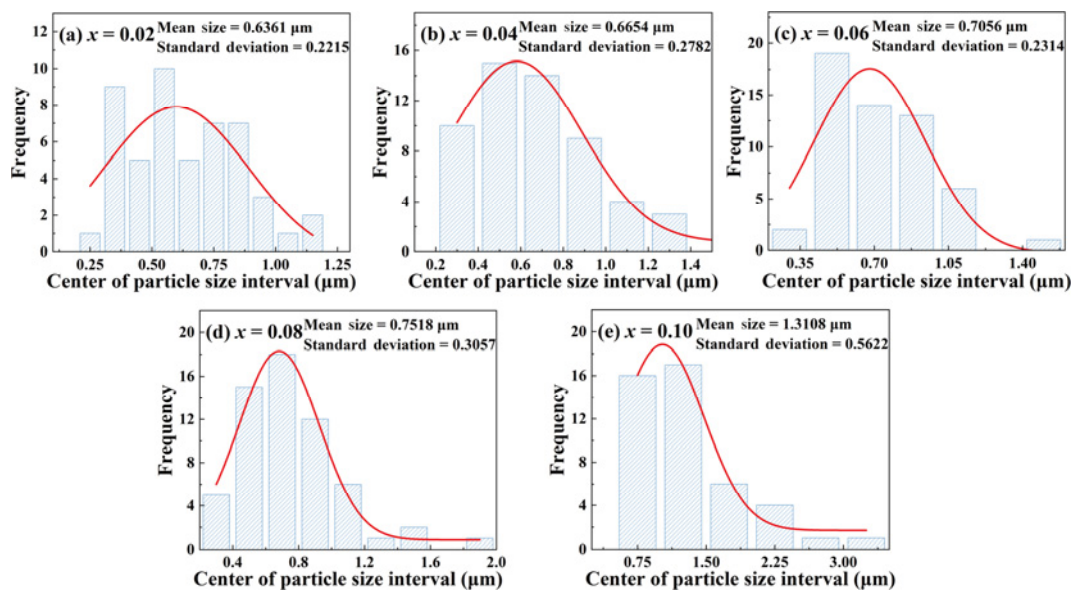

Fig. 5 Grain size distributions of NZ$_{1-x}$T$_x$M (x = 0.02–0.10) ceramics sintered at optimal temperatures.
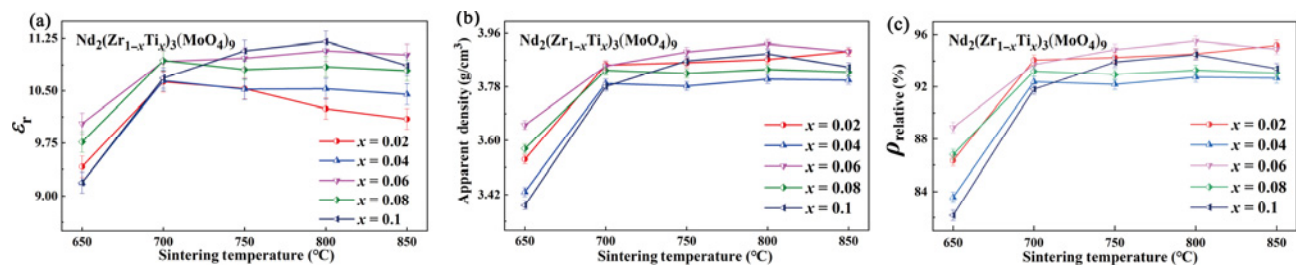

Fig. 6 (a) ε_r, (b) apparent density, and (c) $\rho_{relative}$ of NZ$_{1-x}$T$_x$M (x = 0.02–0.10) ceramics sintered at 650–850 ℃.

linear upward trend as the x increases. The ionic polarizability ($\alpha_{obs.}$) is an important factor affecting the ε_r of the materials, and the relationship is given by Clausius–Mosotti equation [39]:

$$\varepsilon_r = \frac{3}{1 - b\alpha_{obs.}/V} - 2 \tag{4}$$

where $b = 4\pi/3$. According to Eq. (4), the ε_r of the samples is positively correlated with the polarizability

per unit volume ($\alpha_{obs.}/V$). The theoretical polarizability ($\alpha_{theo.}$) of the ceramics can be calculated by Shannon's rule [40].

$$\alpha_{theo.} = \alpha_{obs.} (NZ_{1-x}T_xM)$$

$$= 2\alpha_{obs.}(Nd^{3+}) + 3(1-x)\alpha_{obs.}(Zr^{4+})$$
$$+ 3x\alpha_{obs.}(Ti^{4+}) + 9\alpha_{obs.}(Mo^{6+}) + 36\alpha_{obs.}(O^{2-}) \quad (5)$$

$\alpha (Ti^{4+})$ (2.93 Å³) is less than $\alpha (Zr^{4+})$ (3.25 Å³), and the $\alpha_{theo.}$ of the sample decreases. However, as the x value increased, the V decreased, which led to a linear increase in the $\alpha_{theo.}/V$. The trend of $\alpha_{theo.}/V$ is consistent with that of the $\varepsilon_{corr.}$, which proves that $\alpha_{theo.}/V$ is an important intrinsic factor affecting the dielectric constant of the samples.

According to Batsanov *et al.* [41], the ionicity (f_i) of the chemical bonds plays an important effect on the ε_r of the materials. The f_i of the $NZ_{1-x}T_xM$ ceramics can be calculated by Eqs. (6)–(9) based on the P–V–L theory [42,43].

$$\varepsilon_r = \frac{n_r^2 - 1}{1 - f_i} + 1 \quad (6)$$

$$f_i^\mu = \frac{(C^\mu)^2}{(E_g^\mu)^2} = \frac{(C^\mu)^2}{(E_h^\mu)^2 + (C^\mu)^2} \quad (7)$$

$$(E_h^\mu)^2 = \frac{39.74}{(d^\mu)^{2.48}} \quad (8)$$

$$C^\mu = 14.4b^\mu \exp(-k_s^\mu r_0^\mu)\left[(Z_A^\mu)^* - \frac{n}{m}(Z_B^\mu)^*\right] / r_0^\mu \quad (9)$$

where d^μ is the bond length, n_r is the index of refraction, and the polarization energy (E_g^μ) of the chemical bond (μ) is segmented into the heteropolar part (C^μ) and the homopolar part (E_h^μ). The m and n are the parameters obtained from binary crystal A_mB_n-type crystals. The $(Z_A^\mu)^*$ and $(Z_B^\mu)^*$ are the effective numbers of valence electrons on cation A and anion B, respectively. The $\exp(-k_s^\mu r_0^\mu)$ is the Thomas–Fermi screening factor. The results of the f_i of the $NZ_{1-x}T_xM$ ceramics are exhibited in Table S2 in the ESM. The trend of the f_i of the $NZ_{1-x}T_xM$ ceramics with the x is exhibited in Fig. 8. With the increase of the x, the f_i of the Zr(Ti)–O bonds tends to rise, which is consistent with the $\varepsilon_{corr.}$ of the ceramics. The increase of the f_i of the Zr(Ti)–O bonds after the addition of Zr^{4+} is an important intrinsic factor for the increase of the ε_r of the ceramics.
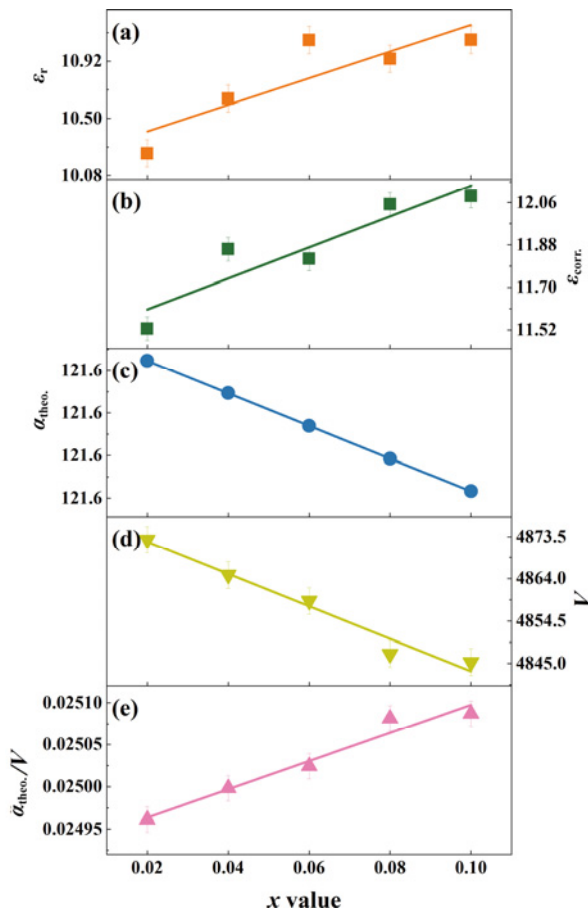

Fig. 7 (a) ε_r, (b) $\varepsilon_{corr.}$, (c) $\alpha_{theo.}$, (d) V, and (e) $\alpha_{theo.}/V$ of $NZ_{1-x}T_xM$ (x = 0.02–0.10) ceramics sintered at optimal temperatures.

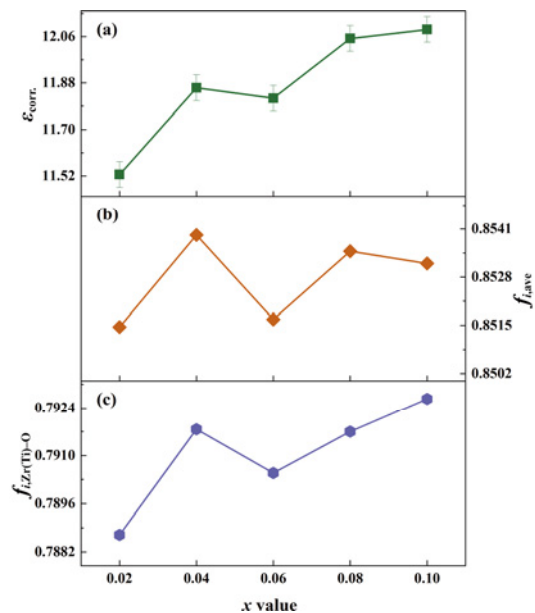**Fig. 8** (a) $\varepsilon_{corr.}$, (b) average ionicity ($f_{i,ave}$) of all bonds, and (c) $f_{i,Zr(Ti)-O}$ of $NZ_{1-x}T_xM$ (x = 0.02–0.10) ceramics sintered at optimal temperatures.

The $Q \cdot f$ is often used to characterize the loss of the MWDCs. Figure 9(a) displays the $Q \cdot f$ of the NZ$_{1-x}$T$_x$M ceramics sintered at various temperatures. With the increase of the sintering temperatures, the $Q \cdot f$ of NZ$_{1-x}$T$_x$M increased from 10,242–15,559 to 49,446–82,525 GHz, and then declined. Both $Q \cdot f$ and ε_r of the NZ$_{1-x}$T$_x$M ceramics are affected by the P of the samples. In addition, the optimal $Q \cdot f$ of NZ$_{0.92}$T$_{0.08}$M is 82,525 GHz, much higher than the $Q \cdot f$ of the NZM (58,942 GHz). Replacing Zr^{4+} with Ti^{4+} is a reliable method to reduce the dielectric loss of the NZM ceramics.

In addition, the chemical bond characteristics, especially the lattice energy (U), also played an important influence on the $Q \cdot f$ of the ceramics. The lattice energy of NZ$_{1-x}$T$_x$M is calculated by Eqs. (10)–(12) [44,45]:

$$U = \sum_\mu (U_{bc}^\mu + U_{bi}^\mu) \qquad (10)$$

$$U_{bc}^\mu = 2100 m \frac{(Z_+^\mu)^{1.64}}{(d^\mu)^{0.75}} f_i^\mu \qquad (11)$$

$$U_{bi}^\mu = \frac{1270(m+n)Z_+^\mu Z_-^\mu}{d^\mu}\left(1 - \frac{0.4}{d^\mu}\right) f_i^\mu \qquad (12)$$

where U_{bc}^μ and U_{bi}^μ represent the covalent part and the ionic part of the lattice energy, respectively, and Z_-^μ and Z_+^μ represent the valence states of the ion. The results of the U of the NZ$_{1-x}$T$_x$M ceramics are exhibited in Table S3 in the ESM. Figure 9(b) shows the calculated results of the lattice energy of the NZ$_{1-x}$T$_x$M ceramics. The lattice energy reflects the size of the binding force between particles in the crystal. The disharmonic vibration of ceramic chemical bonds was reduced with the increase of the lattice energy. The average lattice energy and the $Q \cdot f$ values reached the peak when

the $x = 0.08$. The average lattice energy of the ceramics shows a very similar trend to the $Q \cdot f$.

The τ_f indicates the drift of resonant frequency of the MWDCs at different temperatures. Figure 10(b) displays the variation of the τ_f with the doping content at the optimal sintering temperatures. The τ_f of the NZ$_{1-x}$T$_x$M ceramics is stable at about −13 ppm/℃. According to Eq. (13), the value of τ_f is mainly determined by α_L and τ_ε [46].

$$\tau_f = -\alpha_L - \frac{1}{2}\tau_\varepsilon \qquad (13)$$

where α_L is the thermal expansion coefficient, and τ_ε is the permittivity temperature coefficient. According to Eqs. (14)–(17), the α_L of the NZ$_{1-x}$T$_x$M ceramics is calculated [47].

$$\alpha_L = \sum_\mu F_{mn}^\mu \alpha_{mn}^\mu \qquad (14)$$

$$\alpha_{mn}^\mu = -3.1685 + 0.8376\gamma_{mn} \qquad (15)$$

$$\gamma_{mn} = \frac{kZ_A^\mu N_{CA}^\mu}{U_b^\mu \Delta_A}\beta_{mn} \qquad (16)$$

$$\beta_{mn} = \frac{m(m+n)}{2n} \qquad (17)$$

where F_{mn}^μ represent the ratio of the μ, U_b^μ is the lattice energy for the type-μ bond, k is the Boltzmann constant, and Δ_A, N_{CA}^μ, and Z_A^μ are the periodic constant, the coordination number, and the valence states of the cations, respectively. γ_{mn} and β_{mn} are two parameters in the binary bonding formula. The specific data of the α_L of the NZ$_{1-x}$T$_x$M ceramics are exhibited in Table S4 in the ESM. As shown in Fig. 10(a), the trend of the average α_L ($\alpha_{L,ave}$) is opposite to the values of the τ_f, which is consistent with Eq. (13).
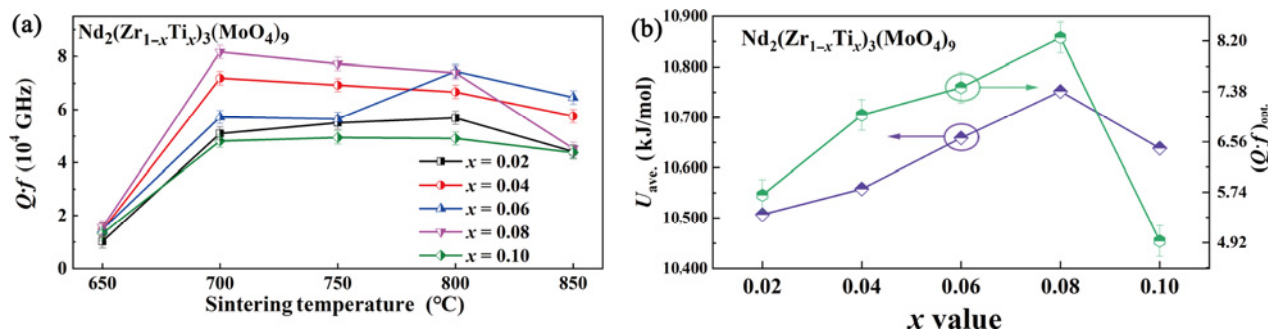

Fig. 9   (a) $Q \cdot f$ and (b) optimal quality factors (($Q \cdot f$)$_{opt.}$) and average lattice energy ($U_{ave.}$) of NZ$_{1-x}$T$_x$M ($x = 0.02$–0.10) ceramics sintered at 650–850 ℃.
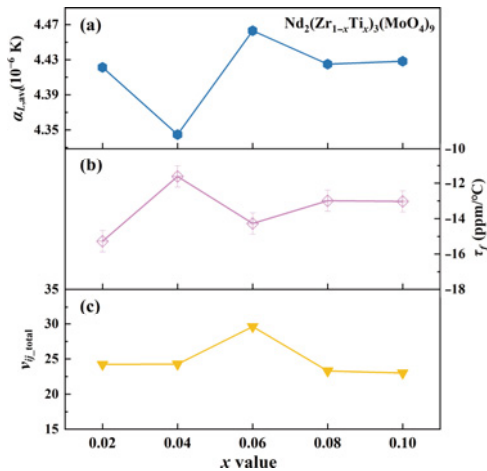
Fig. 10 (a) $\alpha_{L,\mathrm{ave}}$, (b) τ_f, and (c) total bond valences (v_{ij_total}) of $NZ_{1-x}T_xM$ ($x = 0.02$–0.10) ceramics sintered at optimal temperatures.

Furthermore, the bond valences of the atoms are considered a parameter related to the τ_f of the MWDCs. The bond valence can be calculated by Eqs. (18) and (19) [48]:

$$v_{ij\_\mathrm{total}} = \sum v_{ij} \tag{18}$$

$$v_{ij} = \exp\left(\frac{d_0 - d_{ij}}{0.37}\right) \tag{19}$$

where v_{ij_total} represents the sum of all valence states of an atom (v_{ij}), d_0 represents the bond valence parameter, and d_{ij} represents the bond length between the atoms i and j. The specific data of the v_{ij_total} of the $NZ_{1-x}T_xM$ ceramics are exhibited in Table S5 in the ESM. As shown in Fig. 10(c), the trend of the total bond valence of the ceramics is opposite to the τ_f. This phenomenon also exists in $Pr_2(Zr_{1-x}Ti_x)_3(MoO_4)_9$ ceramics and is interpreted as the large bond valence, reducing the restoring force of the ceramics [49].

Moreover, according to Eqs. (20)–(22), the IR radiation spectrometer is employed to study the intrinsic dielectric constant and loss of $NZ_{1-x}T_xM$ [50–52].

$$\varepsilon^*(\omega) = \varepsilon_\infty + \sum_{j=1}^{n} \frac{\omega_{pi}^2}{\omega_{oj}^2 - \omega^2 + j\omega\gamma_j} \tag{20}$$

$$R = \left|\frac{1 - \sqrt{\varepsilon^*(\omega)}}{1 + \sqrt{\varepsilon^*(\omega)}}\right|^2 \tag{21}$$

$$\tan\delta = \frac{\varepsilon''}{\varepsilon'} = \frac{\displaystyle\sum_{j=1}^{n} \Delta\varepsilon_j(\gamma_j\omega)/\omega_{oj}^2}{\varepsilon_\infty + \displaystyle\sum_{j=1}^{n} \Delta\varepsilon_j} \tag{22}$$

where ω_{oj}, ω_{pj}, and γ_j are the eigen frequency, the plasma frequency, and the coefficient of damping, respectively, ε' and ε'' are the real and imaginary parts of the complex dielectric constant, respectively, ε_∞ is the optical dielectric constant, $\varepsilon^*(\omega)$ is the complex dielectric function, ω is the frequency, R is the infrared reflectivity, and $\tan\delta$ is the dielectric loss tangent. Figure 11(a) shows IR reflectivity spectra of the fitted and measured $NZ_{0.92}T_{0.08}M$ samples. The values of the real and imaginary parts of the complex dielectric constant of the sample are exhibited in Figs. 11(b) and 11(c), respectively. There are 24 IR vibration modes exhibited in Table 3. The calculated dielectric constant (ε_0) of the $NZ_{0.92}T_{0.08}M$ ceramic is 7.98, smaller than the measured value (10.94, at 12.82 GHz). The defect phonon scattering included in the ε_r of the ceramic may be one of the reasons. The calculated dielectric loss of the ceramic is 1.13×10^{-4}, which is close to the measured value (1.18×10^{-4}). At microwave frequencies, only the ionic polarization and electron polarization are considered to contribute to the dielectric constant. The ε_∞ of the ceramic is 3.07, which is only 38.47% of the total polarizability contribution, suggesting that the main contribution to the dielectric constant comes from the ionic polarization. In the future, the other electric properties of the $NZ_{1-x}T_xM$ ceramics will be further discussed as those in Refs. [53–55].
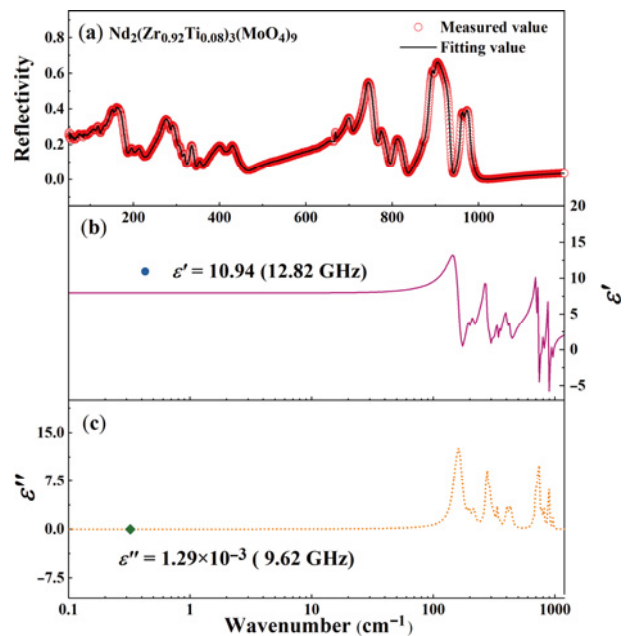

Fig. 11 (a–c) IR reflectivity spectra of fitted (black line) and measured (red circle) values, ε', and ε'' of $NZ_{0.92}T_{0.08}M$ sample, respectively.

Table 3 Results obtained from the fitting of IR reflectivity spectrum of NZ$_{0.92}$T$_{0.08}$M

Mode	ω_{oj} (cm^{-1})	ω_{pj} (cm^{-1})	γ_j (cm^{-1})	$\Delta\varepsilon_j$
1	158.44	225.29	29.32	2.020
2	163.46	45.95	7.62	0.079
3	169.82	66.92	12.62	0.155
4	197.04	51.87	9.67	0.069
5	214.93	87.41	16.93	0.165
6	275.60	192.16	16.71	0.486
7	291.36	137.26	16.10	0.222
8	310.02	122.97	26.77	0.157
9	336.27	91.69	8.55	0.074
10	354.92	55.79	8.88	0.025
11	402.21	163.97	23.31	0.166
12	429.96	178.17	24.12	0.172
13	450.27	87.22	27.39	0.038
14	657.76	116.29	28.68	0.031
15	700.35	355.02	24.84	0.257
16	735.09	452.28	18.87	0.379
17	773.70	181.37	17.59	0.055
18	810.31	244.93	22.48	0.091
19	872.04	112.36	11.42	0.017
20	887.26	377.44	8.78	0.181
21	897.69	155.43	12.24	0.030
22	915.46	64.63	14.97	0.005
23	955.88	170.93	10.65	0.032
24	968.36	48.78	8.49	0.003
NZ$_{0.92}$T$_{0.08}$M	$\varepsilon_\infty = 3.07$	$\varepsilon_0 = 7.98$		

4 Conclusions

In this work, the NZ$_{1-x}$T$_x$M (x = 0.02–0.10) ceramics were fabricated through the conventional solid-phase method. The XRD data exhibit that the NZ$_{1-x}$T$_x$M ceramic solid solution with the $R\bar{3}c$ (167) space group is formed, and the Ti^{4+} substitution does not produce a secondary phase. The lattice volume of the samples decreased linearly with the increase of the substitutions because the ionic radius of Zr^{4+} (0.72 Å) is larger than the ionic radius of Ti^{4+} (0.605 Å). The surface of the NZ$_{1-x}$T$_x$M samples sintered at the optimal temperatures shows the clear grain boundaries and no obvious pores. The uneven distribution of the grain size may deteriorate the dielectric properties of the sample. When x = 0.08 and sintered at 700 ℃, the best

microwave dielectric properties of NZ$_{1-x}$T$_x$M were obtained, including ε_r = 10.94, $Q{\cdot}f$ = 82,525 GHz (at 9.62 GHz), and τ_f = −12.99 ppm/℃. The excellent $Q{\cdot}f$ of the NZ$_{1-x}$T$_x$M ceramics makes it possible to prepare high-performance passive devices. Furthermore, the properties of NZ$_{1-x}$T$_x$M were researched in depth. The decrease of the α_{theo}/V of the ceramics reduced the ε_r. The increase of the f_i of the Zr(Ti)–O bonds is an intrinsic factor for the increase of the ε_r. The average lattice energy of the ceramics plays an important role in the $Q{\cdot}f$. The large bond valence reduces the restoring force of the ceramics, and thus affects the the τ_f. The IR reflectivity spectra demonstrated that the main polarization mechanism of the NZ$_{1-x}$T$_x$M ceramics in the microwave band is the ionic polarization.

Electronic Supplementary Material

Supplementary material is available in the online version of this article at https://doi.org/10.26599/JAC.2023.9220668.

References

[1] Luo WJ, Yan S, Zhou J. Ceramic-based dielectric metamaterials. *Interdiscip Mater* 2022, **1**: 11–27.

[2] Pei CJ, Tan JJ, Li Y, *et al*. Effect of Sb-site nonstoichiometry on the structure and microwave dielectric properties of Li$_3$Mg$_2$Sb$_{1-x}$O$_6$ ceramics. *J Adv Ceram* 2020, **9**: 588–594.

[3] Zhang YH, Wu HT. Crystal structure and microwave dielectric properties of La$_2$(Zr$_{1-x}$Ti$_x$)$_3$(MoO$_4$)$_9$ (0 ⩽ x ⩽ 0.1) ceramics. *J Am Ceram Soc* 2019, **102**: 4092–4102.

[4] Yao GG, Yan JX, Tan JJ, *et al*. Structure, chemical bond and microwave dielectric characteristics of novel Li$_3$Mg$_4$NbO$_8$ ceramics. *J Eur Ceram Soc* 2021, **41**: 6490–6494.

[5] Yang HY, Chai L, Wang YC, *et al*. Matching correlation study of titanium-based ceramics with glass based on dissolution characteristics. *J Eur Ceram Soc* 2022, **42**: 5778–5788.

[6] Bao J, Du JL, Liu LT, *et al*. A new type of microwave

dielectric ceramic based on K$_2$O–SrO–P$_2$O$_5$ composition with high quality factor and low sintering temperature. *Ceram Int* 2022, **48**: 784–794.

[7] Xiang HC, Li CC, Jantunen H, *et al*. Ultralow loss CaMgGeO$_4$ microwave dielectric ceramic and its chemical compatibility with silver electrodes for low-temperature cofired ceramic applications. *ACS Sustain Chem Eng* 2018, **6**: 6458–6466.

[8] Zhang X, Fang ZX, Yang HY, *et al*. Lattice evolution, ordering transformation and microwave dielectric properties of rock-salt Li$_{3+x}$Mg$_{2-2x}$Nb$_{1-x}$Ti$_x$O$_6$ solid-solution system: A newly developed pseudo ternary phase diagram. *Acta Mater* 2021, **206**: 116636.

[9] Hao SZ, Zhou D, Hussain F, *et al*. Structure, spectral analysis and microwave dielectric properties of novel x(NaBi)$_{0.5}$MoO$_4$–(1−x)Bi$_{2/3}$MoO$_4$ (x = 0.2–0.8) ceramics with low sintering temperatures. *J Eur Ceram Soc* 2020, **40**: 3569–3576.

[10] Zhou X, Liu LT, Sun JJ, *et al*. Effects of (Mg$_{1/3}$Sb$_{2/3}$)$^{4+}$ substitution on the structure and microwave dielectric properties of Ce$_2$Zr$_3$(MoO$_4$)$_9$ ceramics. *J Adv Ceram* 2021, **10**: 778–789.

[11] Zhang GQ, Wang H, Guo J, *et al*. Ultra-low sintering temperature microwave dielectric ceramics based on Na$_2$O–MoO$_3$ binary system. *J Am Ceram Soc* 2015, **98**: 528–533.

[12] Zhang GQ, Guo J, He L, *et al*. Preparation and microwave dielectric properties of ultra-low temperature sintering ceramics in K$_2$O–MoO$_3$ binary system. *J Am Ceram Soc* 2014, **97**: 241–245.

[13] Hao SZ, Zhou D, Pang LX, *et al*. Ultra-low temperature co-fired ceramics with adjustable microwave dielectric properties in the Na$_2$O–Bi$_2$O$_3$–MoO$_3$ ternary system: A comprehensive study. *J Mater Chem C* 2022, **10**: 2008–2016.

[14] Zhang YH, Sun JJ, Dai N, *et al*. Crystal structure, infrared spectra and microwave dielectric properties of novel extra low-temperature fired Eu$_2$Zr$_3$(MoO$_4$)$_9$ ceramics. *J Eur Ceram Soc* 2019, **39**: 1127–1131.

[15] Liu WQ, Zuo RZ. Low temperature fired Ln$_2$Zr$_3$(MoO$_4$)$_9$ (Ln = Sm, Nd) microwave dielectric ceramics. *Ceram Int* 2017, **43**: 17229–17232.

[16] Zheng JJ, Xing CF, Yang YK, *et al*. Structure, infrared reflectivity spectra and microwave dielectric properties of a low-firing microwave dielectric ceramic Pr$_2$Zr$_3$(MoO$_4$)$_9$. *J Alloys Compd* 2020, **826**: 153893.

[17] Liu WQ, Zuo RZ. A novel low-temperature firable La$_2$Zr$_3$(MoO$_4$)$_9$ microwave dielectric ceramic. *J Eur Ceram Soc* 2018, **38**: 339–342.

[18] Xing CF, Wu B, Bao J, *et al*. Crystal structure, infrared spectra and microwave dielectric properties of a novel low-firing Gd$_2$Zr$_3$(MoO$_4$)$_9$ ceramic. *Ceram Int* 2019, **45**: 22207–22214.

[19] Tao BJ, Xing CF, Wang WF, *et al*. A novel Ce$_2$Zr$_3$(MoO$_4$)$_9$ microwave dielectric ceramic with ultra-low firing temperature. *Ceram Int* 2019, **45**: 24675–24683.

[20] Tian HR, Jiang L, Du JL, *et al*. Effects of Sn substitution on

the crystal structures, microstructures, and microwave dielectric properties of Ce$_2$Zr$_3$(MoO$_4$)$_9$ ceramics. *Ceram Int* 2021, **47**: 22939–22948.

[21] Bao J, Zhang YP, Wu HT, *et al*. Sintering characteristics, crystal structure and dielectric properties of cobalt–tungsten doped molybdate-based ceramics at microwave frequency. *J Materiomics* 2022, **8**: 949–957.

[22] Guo WJ, Ma ZY, Luo Y, *et al*. Structure, defects, and microwave dielectric properties of Al-doped and Al/Nd co-doped Ba$_4$Nd$_{9.33}$Ti$_{18}$O$_{54}$ ceramics. *J Adv Ceram* 2022, **11**: 629–640.

[23] Shi F, Dong HL. Correlation of crystal structure, dielectric properties and lattice vibration spectra of (Ba$_{1-x}$Sr$_x$)(Zn$_{1/3}$Nb$_{2/3}$)O$_3$ solid solutions. *Dalton Trans* 2011, **40**: 6659–6667.

[24] Feng C, Zhou X, Tao BJ, *et al*. Crystal structure and enhanced microwave dielectric properties of the Ce$_2$[Zr$_{1-x}$(Al$_{1/2}$Ta$_{1/2}$)$_x$]$_3$(MoO$_4$)$_9$ ceramics at microwave frequency. *J Adv Ceram* 2022, **11**: 392–402.

[25] Tian HR, Zhou X, Jiang TY, *et al*. Bond characteristics and microwave dielectric properties of (Mn$_{1/3}$Sb$_{2/3}$)$^{4+}$ doped molybdate based low-temperature sintering ceramics. *J Alloys Compd* 2022, **906**: 164333.

[26] Bao J, Wang YZ, Kimura H, *et al*. Sintering characteristics, crystal structure, and microwave dielectric properties of Ce$_2$[Zr$_{1-x}$(Al$_{1/2}$Nb$_{1/2}$)$_x$]$_3$(MoO$_4$)$_9$ ceramics. *J Alloys Compd* 2022, **925**: 166566.

[27] Yang HY, Zhang SR, Yang HC, *et al*. Usage of P–V–L bond theory in studying the structural/property regulation of microwave dielectric ceramics: A review. *Inorg Chem Front* 2020, **7**: 4711–4753.

[28] Parvez Ahmad MD, Venkateswara Rao A, Suresh Babu K, *et al*. Effect of carbon-doping on structural and dielectric properties of zinc oxide. *J Adv Dielectr* 2020, **10**: 2050017.

[29] Yang LH, Song LW, Li Q, *et al*. Dielectric properties and electrical response of yttrium-doped Bi$_{2/3}$Cu$_3$Ti$_4$O$_{12}$ ceramics. *J Adv Dielectr* 2021, **11**: 2150007.

[30] Zubkov SV. Structure and dielectric properties of solid solutions Bi$_{7-2x}$Nd$_{2x}$Ti$_4$NbO$_{21}$ (x = 0.0, 0.2, 0.4, 0.6, 0.8, 1.0). *J Adv Dielectr* 2021, **11**: 2160018.

[31] Hakki BW, Coleman PD. A dielectric resonator method of measuring inductive capacities in the millimeter range. *IRE Trans Microw Theory Tech* 1960, **8**: 402–410.

[32] Guo HH, Fu MS, Zhou D, *et al*. Design of a high-efficiency and-gain antenna using novel low-loss, temperature-stable Li$_2$Ti$_{1-x}$(Cu$_{1/3}$Nb$_{2/3}$)$_x$O$_3$ microwave dielectric ceramics. *ACS Appl Mater Inter* 2021, **13**: 912–923.

[33] Bi JX, Xing CF, Yang CH, *et al*. Phase composition, microstructure and microwave dielectric properties of rock salt structured Li$_2$ZrO$_3$–MgO ceramics. *J Eur Ceram Soc* 2018, **38**: 3840–3846.

[34] Xing CF, Bao J, Sun YF, *et al*. Ba$_2$BiSbO$_6$: A novel microwave dielectric ceramic with monoclinic structure. *J Alloys Compd* 2019, **782**: 754–760.

[35] Du K, Wang F, Song XQ, *et al*. Correlation between crystal

structure and dielectric characteristics of Ti^{4+} substituted CaSnSiO$_5$ ceramics. *J Eur Ceram Soc* 2021, **41**: 2568–2578.

[36] Klevtsova RF, Solodovnikov SF, Tushinova YL, *et al*. A new type of mixed framework in the crystal structure of binary molybdate Nd$_2$Zr$_3$(MoO$_4$)$_9$. *J Struct Chem* 2000, **41**: 280–284.

[37] Yin CZ, Yu ZZ, Shu LL, *et al*. A low-firing melilite ceramic Ba$_2$CuGe$_2$O$_7$ and compositional modulation on microwave dielectric properties through Mg substitution. *J Adv Ceram* 2021, **10**: 108–119.

[38] Bosman AJ, Havinga EE. Temperature dependence of dielectric constants of cubic ionic compounds. *Phys Rev* 1963, **129**: 1593–1600.

[39] Yang HC, Zhang SR, Yang HY, *et al*. Vibrational spectroscopic and crystal chemical analyses of double perovskite Y$_2$MgTiO$_6$ microwave dielectric ceramics. *J Am Ceram Soc* 2020, **103**: 1121–1130.

[40] Shannon RD. Dielectric polarizabilities of ions in oxides and fluorides. *J Appl Phys* 1993, **73**: 348–366.

[41] Batsanov SS. Dielectric methods of studying the chemical bond and the concept of electronegativity. *Russ Chem Rev* 1982, **51**: 684–697.

[42] Wu ZJ, Meng QB, Zhang SY. Semiempirical study on the valences of Cu and bond covalency in Y$_{1-x}$Ca$_x$Ba$_2$Cu$_3$O$_{6+y}$. *Phys Rev B* 1998, **58**: 958–962.

[43] Yang HY, Zhang SR, Chen YW, *et al*. Crystal chemistry, Raman spectra, and bond characteristics of trirutile-type Co$_{0.5}$Ti$_{0.5}$TaO$_4$ microwave dielectric ceramics. *Inorg Chem* 2019, **58**: 968–976.

[44] Wu HT, Kim ES. Correlations between crystal structure and dielectric properties of high-Q materials in rock-salt structure Li$_2$O–MgO–BO$_2$ (B = Ti, Sn, Zr) systems at microwave frequency. *RSC Adv* 2016, **6**: 47443–47453.

[45] Chen JQ, Fang WS, Ao LY, *et al*. Structure and chemical bond characteristics of two low-ε_r microwave dielectric ceramics LiBO$_2$ (B = Ga, In) with opposite τ_f. *J Eur Ceram Soc* 2021, **41**: 3452–3458.

[46] Guo HH, Zhou D, Liu WF, *et al*. Microwave dielectric properties of temperature-stable zircon-type (Bi,Ce)VO$_4$ solid solution ceramics. *J Am Ceram Soc* 2020, **103**: 423–431.

[47] Zhou X, Ji XL, Liu LT, *et al*. Bond characteristics, sintering behavior and microwave dielectric properties of Ce$_2$[Zr$_{1-x}$(Ca$_{1/3}$Sb$_{2/3}$)$_x$]$_3$(MoO$_4$)$_9$ ceramics. *Ceram Int* 2022,

48: 11056–11063.

[48] Xiao EC, Cao ZK, Li JZ, *et al*. Crystal structure, dielectric properties, and lattice vibrational characteristics of LiNiPO$_4$ ceramics sintered at different temperatures. *J Am Ceram Soc* 2020, **103**: 2528–2539.

[49] Tian HR, Zheng JJ, Liu LT, *et al*. Structure characteristics and microwave dielectric properties of Pr$_2$(Zr$_{1-x}$Ti$_x$)$_3$(MoO$_4$)$_9$ solid solution ceramic with a stable temperature coefficient. *J Mater Sci Technol* 2022, **116**: 121–129.

[50] Yang HC, Zhang SR, Yang HY, *et al*. The latest process and challenges of microwave dielectric ceramics based on pseudo phase diagrams. *J Adv Ceram* 2021, **10**: 885–932.

[51] Zheng JJ, Yang YK, Wu HT, *et al*. Structure, infrared spectra and microwave dielectric properties of the novel Eu$_2$TiO$_5$ ceramics. *J Am Ceram Soc* 2020, **103**: 4333–4341.

[52] Xing C, Li JZ, Wang J, *et al*. Internal relations between crystal structures and intrinsic properties of nonstoichiometric Ba$_{1+x}$MoO$_4$ ceramics. *Inorg Chem* 2018, **57**: 7121–7128.

[53] Bai JW, Yang J, Lv ZF, *et al*. Magnetic and dielectric properties of Ti^{4+}-doped M-type hexaferrite BaFe$_{12-x}$Ti$_x$O$_{19}$ ceramics. *J Inorg Mater* 2021, **36**: 43–48. (in Chinese)

[54] Chen Y, Wang XS, Li YX, *et al*. Dynamic mechanical analysis in the investigation on ferroelectrics. *J Inorg Mater* 2020, **35**: 857–866. (in Chinese)

[55] Guo L, Qiao XJ, Li XZ, *et al*. Dielectric, ferroelectric and piezoelectric properties of Pb(In$_{1/2}$Nb$_{1/2}$)O$_3$–Pb(Ni$_{1/3}$Nb$_{2/3}$)O$_3$–PbTiO$_3$ ternary ceramics near morphotropic phase boundary. *J Inorg Mater* 2020, **35**: 1380–1384.